Article

Inhalable SARS-CoV-2 Mimetic Particles Induce Pleiotropic Antigen Presentation

Atip Lawanprasert, Andrew W. Simonson, Sarah E. Sumner, McKayla J. Nicol, Sopida Pimcharoen, Girish S. Kirimanjeswara, and Scott H. Medina*

Cite This: https://doi.org/10.1021/acs.biomac.1c01447

Read Online

ACCESS | Metrics & More | Article Recommendations | Supporting Information

ABSTRACT: Coronavirus disease 2019 (Covid-19) has caused over 5.5 million deaths worldwide, and viral mutants continue to ravage communities with limited access to injectable vaccines or high rates of vaccine hesitancy. Inhalable vaccines have the potential to address these distribution and compliance issues as they are less likely to require cold storage, avoid the use of needles, and can elicit localized immune responses with only a single dose. Alveolar macrophages represent attractive targets for inhalable vaccines as they are abundant within the lung mucosa (up to 95% of all immune cells) and are important mediators of mucosal immunity, and evidence suggests that they may be key cellular players in early Covid-19 pathogenesis. Here, we report inhalable coronavirus mimetic particles (CoMiP) designed to rapidly bind to, and be internalized by, alveolar macrophages to deliver nucleic acid-encoded viral antigens. Inspired by the SARS-CoV-2 virion structure, CoMiP carriers package nucleic acid cargo within an endosomolytic peptide envelope that is wrapped in a macrophage-targeting glycosaminoglycan coating. Through this design, CoMiP mimic several important features of the SARS-CoV-2 virion, particularly surface topography and macromolecular chemistry. As a result, CoMiP effect pleiotropic transfection of macrophages and lung epithelial cells in vitro with multiple antigen-encoding plasmids. In vivo immunization yields increased mucosal IgA levels within the respiratory tract of CoMiP vaccinated mice.
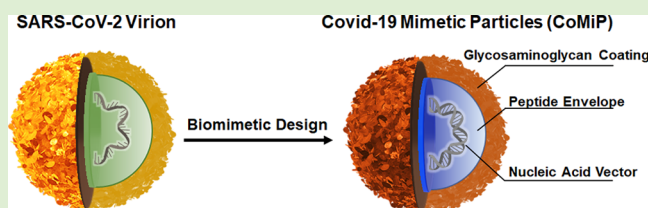
1. INTRODUCTION

Coronavirus disease 2019 (Covid-19), caused by severe acute respiratory syndrome coronavirus 2 (SARS-CoV-2), initiates in the lower respiratory tract of humans, particularly within the alveolar tissue.[1,2] It is now appreciated that before infecting alveolar epithelial cells, SARS-CoV-2 first encounters alveolar macrophages abundantly present at the epithelial surface (90—95% of resident immune cells).[3–5] Unfortunately, angiotensin-converting enzyme 2 (ACE2), the binding receptor of the SARS viral spike protein,[6,7] is expressed on the surfaces of activated alveolar macrophages.[8,9] Thus, macrophage infection is likely the first step of Covid-19 pathogenesis.[10,11] This generates contradictory biologic effects, initiating both important antiviral defense mechanisms while also yielding "Trojan horse" macrophage hosts that promote the anchorage of SARS-CoV-2 within the pulmonary parenchyma. Additionally, migration of virus-containing macrophages out of the lung may spread the pathogen to distal organs and lead to systemic infection.[9,12] This is referred to as the "macrophage paradox", describing the ability of the pathogen to replicate within the very cells equipped to destroy them.[5,13]

Given the importance of alveolar macrophages in Covid-19 pathogenesis, we speculate that targeted delivery of SARS-CoV-2 antigens to these key professional antigen presenting cells via inhalable vaccines may yield potent prophylactic mucosal immunity. Such a strategy has several advantages over traditional systemic vaccination. In addition to being needle-free and minimally invasive, direct pulmonary antigen delivery may reduce side effects and lead to the production of antigen-specific secretory IgA antibodies at the respiratory mucosa.[14–18] This would elicit local immunity at the primary site of infection, where SARS-CoV-2 could be subsequently rapidly neutralized and eliminated without the inflammatory response characteristic of systemic vaccination.

To test this premise, we developed inhalable Covid-19 mimetic particles (CoMiP) designed to be rapidly phagocytosed by macrophages to preferentially deliver viral antigens. Given the use of nucleic acid vectors (e.g., mRNA) in many current Covid-19 vaccines, we elected to deliver antigen-encoding plasmids as an initial model system. Inspired by the SARS-CoV-2 virion, CoMiP carriers package the nucleic acid cargo within a peptide envelope that is coated by a glycosaminoglycan surface layer (Figure 1A). Here, the endosomolytic peptide poly-L-lysine (PLL) electrostatically assembles with the anionic nucleic acid to form a polyplex,
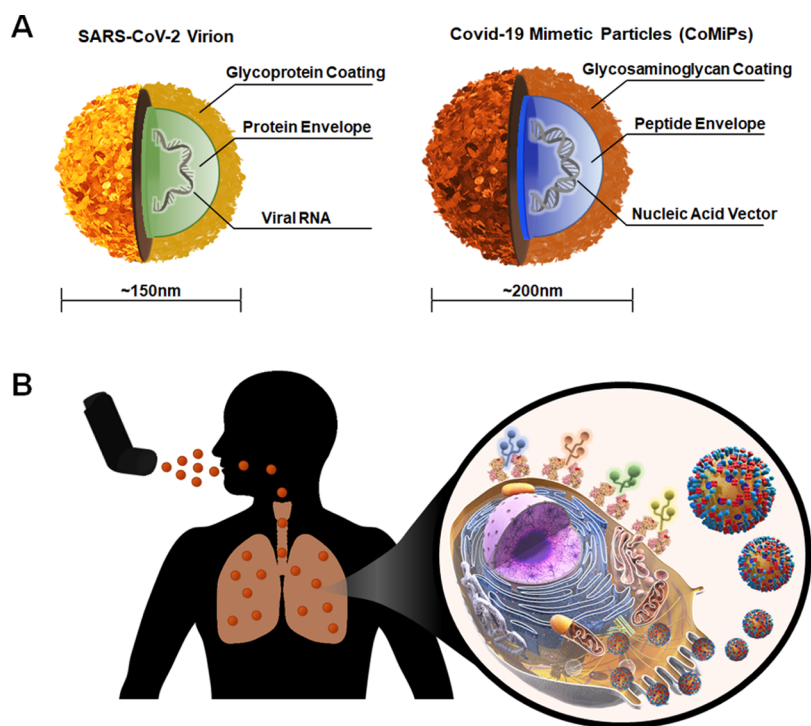
Figure 1. (A) Schematic representation of the structural and compositional similarities between the SARS-CoV-2 virion (left) and rationally designed CoMiP (right). (B) CoMiP carriers engage CD44 receptors on the surfaces of alveolar macrophages in the lung tissue to gain intracellular entry. Cytoplasmic delivery and expression of nucleic acid cargo lead to the presentation of various encoded SARS-CoV-2 antigens to stimulate local mucosal immunity.

which is subsequently coated by the anionic carbohydrate, hyaluronic acid (HA). This versatile platform allows for the pleiotropic transfection of macrophages and lung epithelial cells with multiple antigen-encoding plasmids (Figure 1B). Through several in vitro and in vivo studies, we show that CoMiP aerosols successfully transfect lung cells with pDNA vectors and that antigen expression within alveolar macrophages leads to increased respiratory mucosal IgA levels in immunized mice.

2. MATERIALS AND METHODS

2.1. Materials. PLL 0.1% (w/v) in water (PLL) was obtained from Alamanda Polymers (Huntsville, AL). Sodium hyaluronate, 100k MW (HA), was purchased from Lifecore Biomedical (Chaska, MN). Nuclease-free water, bovine serum albumin (BSA), 2-mercaptoethanol (BME), and dimethyl sulfoxide (DMSO) were obtained from Fisher Scientific (Hampton, NH). The Strep-Tactin XT conjugated to Dy-549 (Strep-Tactin-Dy549) antibody was purchased from IBA (Göttingen, Germany). Hoechst 33342, Transferrin from human serum, Texas Red Conjugate (TransferrinRED-Texas Red), ProLong Diamond Antifade Mountant with DAPI, Lipofectamine 3000 transfection reagent, DYKDDDDK Tag Monoclonal Antibody (FG4R), and DyLight 550 (Anti-Flag-Dy550) were from Invitrogen (Waltham, MA). THP-1 cell lines, the vascular cell basal medium, and an endothelial cell growth kit were purchased from ATCC (Manassas, VA). Fetal bovine serum (FBS) was purchased from HyClone (Logan, UT). The RPMI-1640 cell medium was purchased from Lonza (Basel, Switzerland). L-Glutamine 200 mM 100× (L-GLN) was purchased from VWR (Radnor, PA). 0.25% Trypsin, 2.21 mM EDTA, 1× solution was purchased from Corning (Corning, NY). Triton-X100 and Tween-20 were purchased from Sigma-Aldrich (St. Louis, MO). Paraformaldehyde 4% solution was purchased from ChemCruz Scientific (Dallas, TX). 3-(4,5-Dimethylthiazol-2-yl)-2,5-diphenyltetrazolium bromide (MTT) was obtained from Chem-Impex (Wood Dale, IL). Human umbilical vein endothelial cells (HUVECs) and the RAW264.7 cell line were generously gifted by the laboratory of Dr. Yong Wang within the Pennsylvania State University Department of Biomedical Engineering.

2.2. Plasmids. The purified pEGFP vector was a generous gift from the laboratory of Dr. Angela Pannier at the University of Nebraska, Lincoln, Department of Biological Systems Engineering. pCMV14-3X-Flag-SARS-CoV-2 S was a gift from Zhaohui Qian (Addgene plasmid #145780; http://n2t.net/addgene:145780; RRID: Addgene_145780). pLVX-EF1alpha-SARS-CoV-2-E-2xStrep-IRES-Puro was a gift from Nevan Krogan (Addgene plasmid #141385; http://n2t.net/addgene:141385; RRID: Addgene_141385). pLVX-EF1alpha-SARS-CoV-2-M-2xStrep-IRES-Puro was a gift from Nevan Krogan (Addgene plasmid #141386; http://n2t.net/addgene:141386; RRID: Addgene_141386). pLVX-EF1alpha-SARS-CoV-2-N-2xStrep-IRES-Puro was a gift from Nevan Krogan (Addgene plasmid #141391; http://n2t.net/addgene:141391; RRID: Addgene_141391). pcDNA3-SARS-CoV-2-S-RBD-sfGFP was a gift from Erik Procko (Addgene plasmid #141184; http://n2t.net/addgene:141184; RRID: Addgene_141184). SARS-CoV-2 protein plasmids were obtained as bacterial agar stab, cultured following Addgene protocols and purified using a QIAGEN Plasmid MIDI Kit (QIAGEN; Germantown, MD).

2.3. CoMiP Formation and Particle Characterization. CoMiP are synthesized by adding 20−200 μg of plasmid into a 3 mL aqueous solution of 0.02% w/v PLL and incubated at room temperature for 30 min to form plasmid + PLL polyplexes. A 200 μL volume of 28.68 mg/mL 100 kDa HA was then added to the solution to allow for self-assembly of CoMiP. In experiments where a high quantity of particles was needed, a 667 μL volume of HA solution was electrosprayed (24 kV, 0.1 mL/min) into the plasmid + PLL bath, following a previously validated protocol.[19] In either case, the mixed solution was gently rocked at 37 °C for 1 h to allow complete CoMiP assembly. Particles were purified via dialysis (300k MWCO) in nuclease-free water overnight and lyophilized, and dry powder was stored at −20 °C until use.

To assess particle formation, scanning electron microscopy (SEM) and dynamic light scattering (DLS) techniques were deployed at each

step of encapsulation. For SEM, 10 μL solutions of free pGFP DNA, pGFP + PLL polyplexes, or pGFP-loaded CoMiP (CoMiP_GFP) were deposited onto specimen stubs and air-dried in a 37 °C oven. Images were taken on a Zeiss SIGMA VP-FESEM (White Plains, NY) with a 5.00 kV energy. In parallel, DLS and zeta potential measurements (Zetasizer; Malvern, PA) were performed by diluting samples into 1 mL ultrapure water in polystyrene microcuvettes (DLS) or disposable folded capillary cells (zeta) at a 1:10 dilution from the stock. Colloidal stability of CoMiP was determined from these DLS experiments. All data were collected at 25 °C with three independent replicates with the sample position and attenuation optimized by the instrument.

Loaded plasmid concentrations were assessed by diluting CoMiP in pre-warmed (37 °C) 1× TNE buffer to a final concentration of 0.1 mg/mL. A 25 μL sample was then mixed with 75 μL of 1× TNE buffer and 100 μL of 0.2 μg/mL Hoechst 33342 solution before addition to 96-well black plates for fluorescence quantification (λ_{ex} = 350 nm, λ_{em} = 470 nm) on a BioTek Cytation 3 microplate reader (Winooski, VT). Plasmid concentrations were calculated relative to fluorescent calibration curves, and the results were normalized to unloaded CoMiP as a blank. The final plasmid mass yielded from CoMiP loading was then calculated using the following equation

$$\text{plasmid mass yielded}(\mu g)$$
$$= \frac{[\text{final plasmid}](\mu g/mL)}{0.1\frac{mg_{CoMiP}}{mL}} \times \text{mass}_{total,lyophilized\ CoMiP}(mg)$$

Percent loading was calculated from plasmid mass yielded using the following equation

$$\% \text{ Loading} = \frac{\text{plasmid mass yielded}(\mu g)}{\text{plasmid mass added}(\mu g)} \times 100\%$$

Loading efficiencies were calculated from ≥3 independent experiments.

2.4. Cell Culture. The THP-1, human macrophage, cell line was cultured in RPMI-1640 supplemented with 10% v/v FBS, 2 mM L-GLN, and 1× BME. The HUVEC cell line was cultured in the vascular cell basal medium supplemented with 5 ng/mL rhVEGF, 5 ng/mL rh EGF, 5 ng/mL rh FGF basic, 15 ng/mL rh IGF-1, 10 mM L-glutamine, 0.75 U/mL heparin sulfate, 1 μg/mL hydrocortisone hemisuccinate, 2% v/v FBS, and 50 μg/mL ascorbic acid. The RAW264.7 (−) NO cell line was cultured in RPMI-1640 supplemented with 10% v/v FBS and 2 mM L-GLN. All cells were cultured in 5% CO_2 and a 37 °C high-humidity incubator.

2.5. In Vitro Uptake and Transfection. For reporter studies utilizing pGFP-loaded CoMiP (CoMiP_GFP), human THP-1 monocytes were seeded onto Lab-Tek II 8-well chamber slides at 5 × 10⁴ cells/well and polarized to an Mø phenotype by addition of 200 nM PMA. After overnight incubation, the supernatant was removed and replaced with CoMiP_GFP samples diluted into complete growth media to achieve a final concentration of 0.3 mg/mL. A transferrin_RED-Texas Red solution was then added at a concentration of 25 μg/mL, and samples were incubated for 1 h. Treatment media were then removed, and cells were fixed via addition of 200 μL of 4% PFA for 15 min. Samples were then washed with phosphate-buffered saline (PBS) twice (200 μL), and the nucleic acid marker, 10 μg/mL Hoechst 33342, was added to each well (15 min, 200 μL). The unreacted dye was washed with 200 μL of PBS buffer twice. Slides were then mounted using ProLong Diamond Antifade Mountant and placed in a 4 °C fridge overnight to allow polymerization. Confocal imaging was performed using an Olympus FluoView 1000 (Tokyo, Japan) confocal microscope with predefined filters for Texas Red, DAPI, and GFP fluorophores.

Flow cytometry studies utilized PMA-induced Mø THP-1 monocytes following the procedure discussed above. 10 × 10⁴ cells/well were seeded in 24-well plates, induced overnight, and then treated with 0.2 mg/mL lyophilized CoMiP_GFP in complete growth media. Blank media were used for untreated controls. After a 96 h incubation, Mø-THP1 cells were retrieved by trypsinization (150 μL, 10 min), diluted in 650 μL of PBS buffer containing 1× BME, and

centrifuged (400 rcf, 5 min) to pellets. Cell samples were then resuspended in fresh PBS buffer containing 1× BME, and flow cytometry analysis was performed on a Luminex Guava easyCyte (Austin, TX). Gating and analysis were performed using FlowJo 10.8 software (BD Biosciences; Franklin Lakes, NJ).

2.6. SARS-CoV-2 Antigen In Vitro Expression. RAW264.7 cells were seeded at 5 × 10⁴ cells/well in a 12-well plate and incubated overnight to adhere. Growth media were then replaced with 1 mL treatment media containing CoMiP_S, CoMiP_E, CoMiP_M, or CoMiP_N (CoMiP loaded with S, E, M, and N plasmid DNA, respectively) diluted from the lyophilized stock to achieve a 0.05 mg/mL particle concentration. Blank media were included as a negative control. Positive controls received an equivalent concentration of plasmid delivered using Lipofectamine 3000, with complexation performed following manufacturer protocols. After a 72 h incubation, treated cells were retrieved by cell scraping into a 2 mL centrifuge tube and centrifuged (300 rcf, 5 min) to pellets, and the diluent was replaced with 1 mL of 0.01% PFA. After a 15 min incubation, 100 μL 0.1% Triton-X100 was added to the tube and incubated for an addition of 15 min to permeabilize. The fixed cells were then centrifuged and washed with 0.1% Triton-X100 and centrifuged again before adding an appropriate fluorescently conjugated antibody in 3% BSA PBS (1:500). Anti-Flag-Dy550 was used for S plasmid, and Strep-Tactin-Dy549 was used for E, M, and N plasmids. Samples were incubated for 30 min on ice to allow complete antibody binding, followed by centrifugation (400 rcf, 15 min) and resuspension of the pellet in before flow cytometry analysis (BD LSR-Fortessa).

In parallel experiments, antigen expression for each construct was evaluated via confocal microscopy. RAW264.7 cells were seeded at 5 × 10³ cells/well in eight-well chamber slides and treated with plasmid-loaded CoMiP following the protocol described above. After a 72 h incubation, cells were washed twice with PBS twice before fixing with 4% PFA for 15 min, followed by permeabilization using 0.1% Triton-X100 for 15 min. Cells were then washed twice and blocked with 1% BSA in PBS for 1 h. The blocking solution was replaced with the appropriate fluorescent conjugated antibody solution, as described above. Samples were washed again with PBS before mounting using ProLong Diamond Antifade Mountant with DAPI. Antigen production was quantified from confocal micrographs by measuring fluorescent intensity using ImageJ ($n \geq 30$).

2.7. In Vitro Biocompatibility. PMA-induced Mø THP-1 monocytes and HUVECs were seeded at 1.5 × 10⁴ and 5 × 10³ cells/well, respectively, in 96-well plates and allowed to adhere overnight. Growth media containing 0.0001−10 mg/mL unloaded CoMiP were then added and incubated for 24 h for HUVECs or 48 h for THP-1 cells. Blank growth media and media containing 20 v/v % DMSO were included as negative and positive controls, respectively. After treatment, the supernatant was removed and replaced with 0.5 mg/mL MTT in growth media. Cells were incubated for 3 h to allow MTT conversion, followed by addition of 100 μL of DMSO and incubation at 37 °C for 15 min to dissolve the formazan product. Absorbance (λ = 590 nm) was read using a Cytation 3 Plate Reader, and percent cell viability was calculated using the below equation

$$\% \text{Viability} = \frac{\lambda_{treatment} - \lambda_{positive\ control}}{\lambda_{negative\ control} - \lambda_{positive\ control}} \times 100\%$$

Viability data were collected from $n \geq 3$ independent measurements and reported as average ± standard deviation.

2.8. In Vivo Immunization. To optimize plasmid loading for in vivo studies, CoMiP samples were prepared using 5, 100, and 200 ng of S pDNA in the bath solution. After completing CoMiP formation and lyophilization, the percentage loading was measured as described earlier. Expression efficiency was assayed as described in methods Section 2.5.

All animal experiments were conducted in accordance with the Institutional Animal Use and Care Committee guidelines at the Pennsylvania State University. C57BL/6 (wildtype) mice, approximately 8 weeks old, were maintained on standard chow diet. Mice were anesthetized with isoflurane and intranasally vaccinated with 10
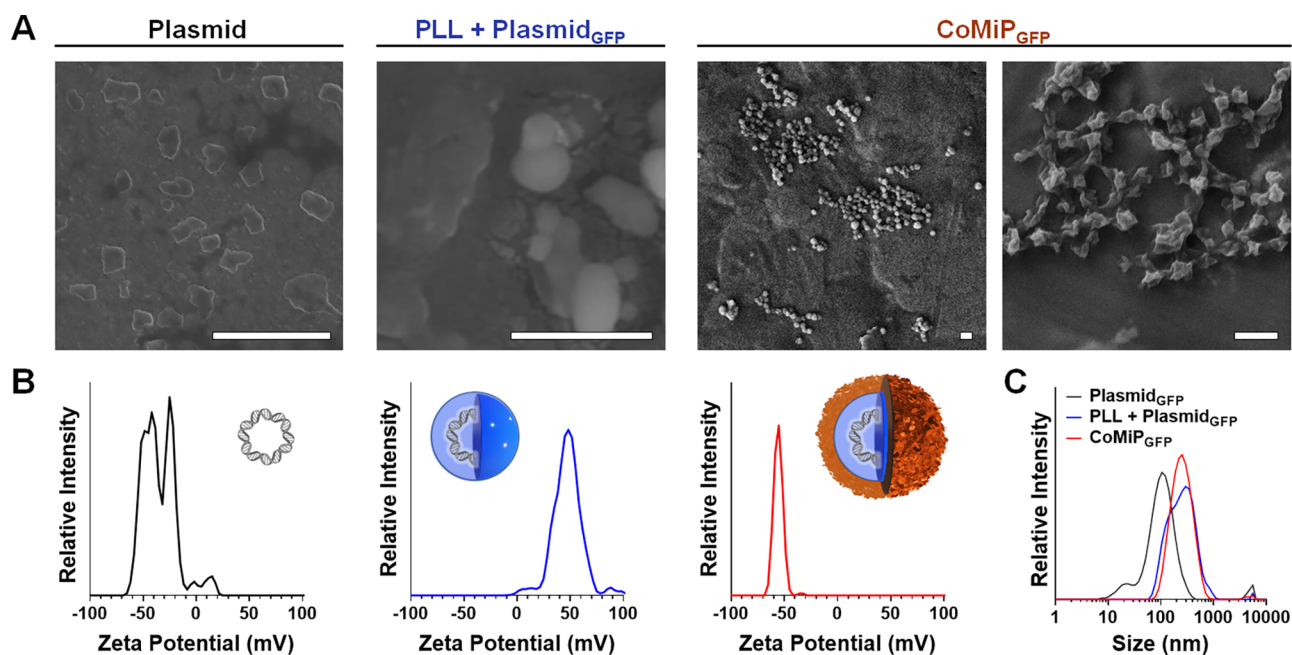
Figure 2. Physicochemical characterization of CoMiP. (A) Representative SEM images and (B) zeta potential measurements of each step in the sequential CoMiP assembly process. Shown are data collected for free eGFP-encoding plasmids (left, black), PLL + plasmid polyplexes (middle, blue), and CoMiP formed upon addition of HA polysaccharides (right, orange). Scale bars in panel A represent 1 μm. (C) Particle size of free plasmids, PLL + plasmid polyplexes, or plasmid-encapsulated CoMiP, as determined by DLS.
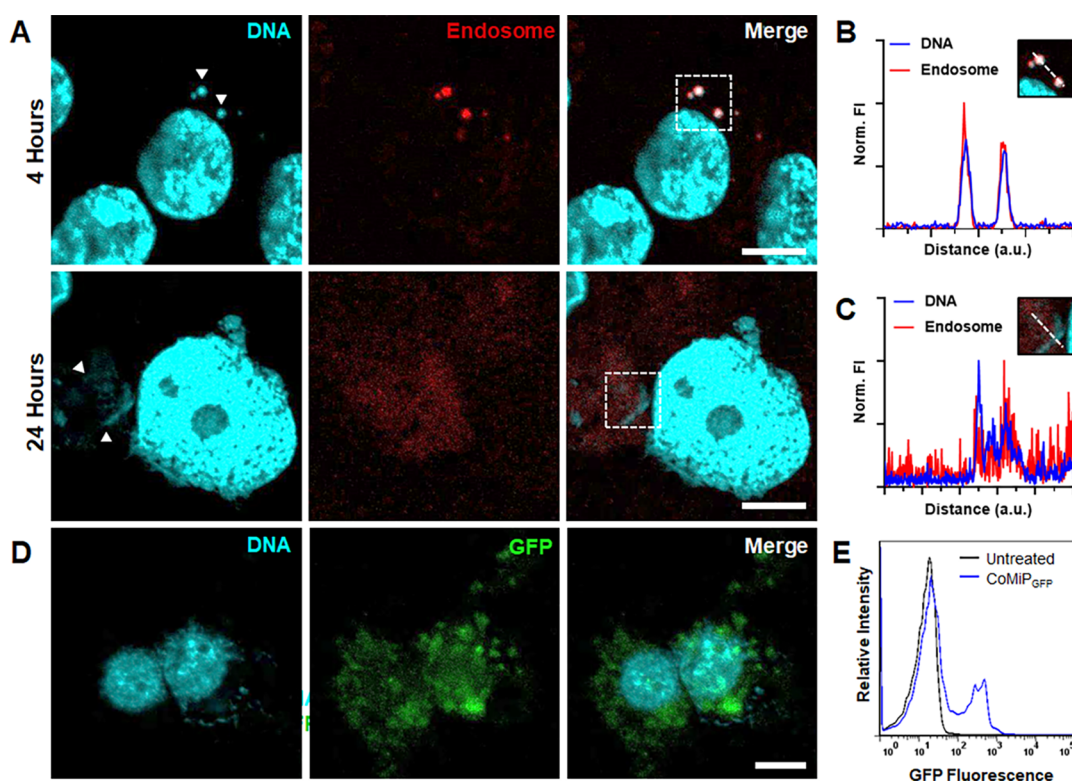

Figure 3. CoMiP uptake and cellular fate. (A) Confocal micrographs of Mø-THP-1 cells 4 h (top) and 24 h (bottom) after treatment with CoMiP loaded with a GFP-encoding plasmid (CoMiP$_{GFP}$). Endosomes are labeled with transferrin$_{Texas Red}$ (red), and DAPI is used to stain both the delivered plasmid and nuclear DNA (cyan). White arrows in the DNA column delineate extranuclear plasmids. (B,C) Fluorescence surface overlays of endosomal (red) and DNA (cyan) signals (B) 4 h and (C) 24 h after CoMiP$_{GFP}$ uptake in regions of interest (A, white dashed box). Inset: Fluorescence intensity measurements collected across a specified region (white dashed line) using ImageJ software. (D) Confocal micrographs of GFP expression in CoMiP$_{GFP}$-treated THP-1 cells 72 h after transfection. (E) Representative flow cytometry results of inactivated THP-1 cells before (untreated, black) and 72 h after (blue) treatment with CoMiP$_{GFP}$. All scale bars = 10 μm.
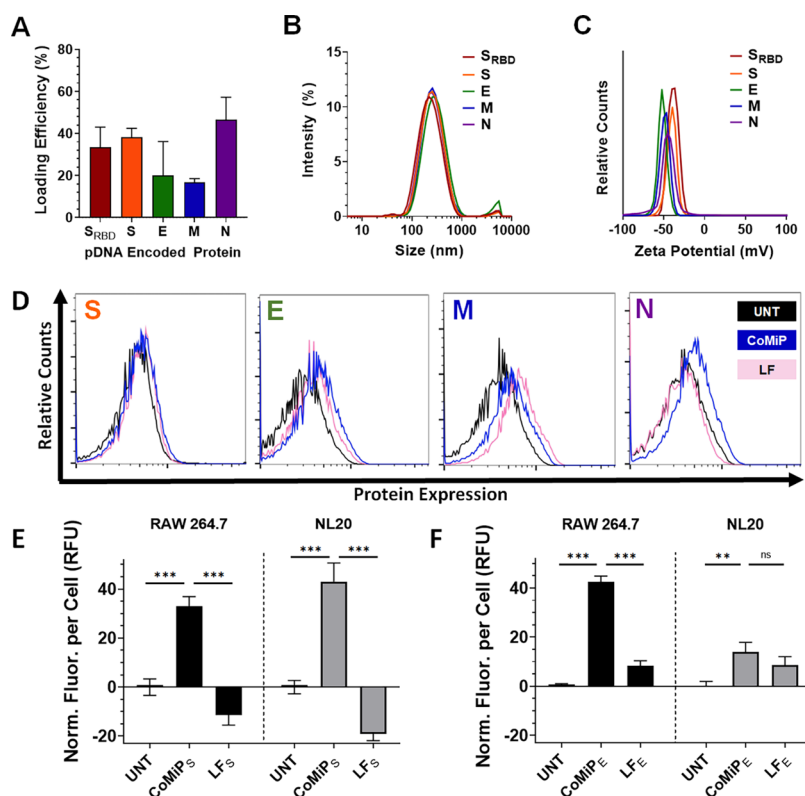
Figure 4. Encapsulation, delivery, and expression of SARS-CoV-2-encoded antigens via plasmid-loaded CoMiP. (A) Loading efficiency of five therapeutic plasmid candidates encoding for the receptor binding domain (S_{RBD}) or full-length spike protein as well as the envelope (E), membrane (M), and nucleocapsid (N) SARS-CoV-2 virion proteins. (B) Size distribution and (C) zeta potential measurements of CoMiP loaded with each pDNA construct. (D) Representative flow cytometry histograms of SARS-CoV-2 protein expression in RAW264.7 murine macrophages before (untreated, black) and 72 h after delivery of S, E, M, and N plasmids via CoMiP carriers (blue) or the control transfection reagent Lipofectamine$_{3000}$ (LF, pink). (E,F) Quantification of antigen expression, in relative fluorescence units, 72 h after transfection of RAW264.7 murine macrophages (black bars) and NL20 human lung epithelial cells with S and E plasmids (E and F, respectively) delivered via CoMiP or LF. S and E plasmid-loaded constructs are identified as CoMiP$_S$ and CoMiP$_E$, respectively. Quantification performed using a fluorescence detection antibody (see Methods), with cellular fluorescence intensity normalized to non-transfected controls. Statistical significance denoted by n.s. = not significant, $**p < 0.01$, $***p < 0.001$.

mg/mL CoMiP$_S$ on day 0, followed by a booster vaccination on day 14. Blood was collected via mandibular cheek bleed on days 14 and 28 post vaccination for enzyme-linked immunoassay (ELISA). The bronchoalveolar lavage fluid (BALF) was collected as previously described.[20] Following BALF collection, lungs were inflated with 4% PFA and stored at room temperature for histological analysis.

2.9. Enzyme-Llinked Immunoassay. Following harvest, blood was allowed to clot and centrifuged (15,000 rpm, 15 min) to isolate serum. Serum was stored at −80 °C until time of use. In a typical ELISA experiment 96-well plates were coated with 100 ng/well of recombinant spike protein (NovusBio, #NBP2-90982) in sodium bicarbonate buffer (pH 9.4) and incubated overnight at 4 °C. Plates were washed in 1× PBS + 0.1% Tween20 and blocked with 1× PBS + 10% FBS for 2 h at room temperature. Following washing with the blocking buffer (1× PBS + 10% FBS), twofold serum dilutions or undiluted BALF was added (100 μL) to the wells in duplicate and incubated at 4 °C overnight. Following wash, 100 μL/well of biotinylated Rabbit anti-mouse IgG-biotin or IgA-HRP was added at a dilution of 1:5000 or 1:500 in PBS, respectively, and incubated overnight at 4 °C. Plates were washed with PBS, a Streptavidin-HRP antibody (1:5000) was added, and the plate was incubated for 20 min at room temperature. Following a PBS wash, the ABTS substrate (SouthernBiotech, 0202-01) was added at 100 μL/well and the plate was allowed to develop. Following color development, optical density was read at 405 nm on a Molecular Devices SpectraMax iD3.

2.10. Statistical Analysis. Statistical differences between data sets were analyzed using unpaired, one-tailed Student's t-test with $n \geq 3$ unless otherwise stated. All statistical analyses were performed using

GraphPad Prism 9 software. Statistical significance is denoted by n.s. = not significant, $*p \leq 0.05$, $**p \leq 0.01$, $***p \leq 0.001$.

3. RESULTS AND DISCUSSION

3.1. Design and Characterization of Viral Mimetic CoMiP. Initial loading studies employed a model eGFP-encoding plasmid to optimize the formulation of CoMiP in vitro. The GFP plasmid was first mixed with PLL to form nanoscale polyplexes. SEM and zeta potential measurements confirmed that this led to the formation of amorphous, cationic complexes (Figure 2A,B) that were approximately 200 nm in diameter (Figure 2C). Addition of the anionic carbohydrate HA led to the formation of spiky nanoparticles that resemble the size (∼150 nm) and surface topography of the SARS-CoV-2 virion (Figure 2A, right).[21−23] Inversion of the particle surface charge to an electronegative potential confirms the presentation of anionic HA at the CoMiP surface (Figure 2B, right). This suggests that the carbohydrate is available to be recognized by CD44 receptors on the surface of macrophages to mediate rapid CoMiP uptake,[19,24,25] an assertion we next tested via time-dependent fluorescence microscopy studies.

3.2. Macrophage Uptake and Intracellular Fate of CoMiP Carriers. Cellular internalization and trafficking of eGFP-encoding CoMiP (CoMiP$_{GFP}$) were evaluated in human THP-1 monocytes polarized to an Mø macrophage phenotype

to mimic naïve alveolar immune cells (Figure 3). Mø macrophages were incubated with CoMiP$_{GFP}$ for 4 and 24 h and co-stained with fluorescently labeled transferrin to visually track endocytic vesicles. Confocal micrographs shown in Figure 3A indicate that at early incubation times (4 h), CoMiP carriers are internalized into macrophages and sequestered within endosomes, as indicated by co-localization of plasmid DNA and transferrin signals (Figure 3B). Conversely, at 24 h, the endocytic label (red) is observed diffusely within the cell cytoplasm and more spatially separated from the delivered pDNA signal (Figure 3C). Collectively, this suggests that CoMiP are initially internalized by receptor-mediated endocytosis, followed later by endosomal escape to deliver pDNA cargo to the cytoplasm. The cytosolic plasmids subsequently enter the nucleus for transcription. This endosomolytic behavior of the CoMiP carrier is likely due to the ability of the incorporated PLL to buffer endosomal acidification and form polyplexes with endosomal lipids.[26] Together, this leads to endo-membrane poration and permeabilization, ultimately allowing cytoplasmic escape of the delivered plasmids and expression of encoded GFP. This is further supported by representative confocal microscopy (Figure 3D) and flow cytometry (Figure 3E) results demonstrating production of the encoded fluorescent protein 72 h after CoMiP uptake. Flow cytometry results show that >20% of treated THP-1 macrophages were successfully transfected. This is significant as macrophages are considered hard-to-transfect cells, having evolved to engage immune responses and clearance mechanisms against foreign nucleic acids. Exemplifying this, several recent studies have reported transgene expression efficiencies of ≤10% following non-viral plasmid transfection of human macrophages.[27,28] While electroporation can improve the THP-1 transfection efficiency, it is often offset by significant cell losses (≥60% cell death).[29−32] As demonstrated later, delivery of SARS-CoV-2 antigens via plasmid-loaded CoMiP vectors maintains ≥70% viability of transfected macrophages.

3.3. Pleiotropic In Vitro Presentation of SARS-CoV-2 Antigens. Next, we selected a panel of plasmids that encode for all four of the SARS-CoV-2 structural proteins, including spike (S), envelope (E), membrane (M), and nucleocapsid (N).[33−35] For the S protein, we included two transgene candidates that encode either the receptor binding domain (S$_{RBD}$[36]) or full-length (S) spike protein. Quantification of loading efficiency demonstrated that 17−47% of available plasmid cargo was successfully encapsulated into the assembled particles (Figure 4A). Particle size and surface charge were unaffected by the identity of the loaded plasmids, with all five formulations showing a ~250 nm hydrodynamic radius and a −50 mV surface charge (Figure 4B,C). This closely matches the size and surface charge of eGFP-plasmid loaded particles (Figure 2), suggesting that CoMiP can be loaded with a variety of nucleic acid cargoes possessing diverse physicochemical properties. Additionally, a highly electronegative surface charge allows CoMiP carriers to maintain colloidal stability and avoid Oswald ripening-mediated precipitation during long-term storage (Supporting Information Figure S1).

Follow-up studies evaluated the transfection of RAW264.7 murine macrophages 72 h after treatment with each CoMiP formulation (Figure 4D). RAW264.7 cells were selected for these experiments to evaluate transfection in a species appropriate cell line for future murine in vivo studies. Preliminary confocal microscopy assays confirmed that similar

to THP-1 cells (Figure 3), plasmid-loaded CoMiP were rapidly internalized into RAW 264.7 cells and that the delivered plasmids are trafficked to the cytosol (Supporting Information Figure S2). Representative transfection results in Figure 4D show that transgene expression was modestly higher in RAW264.7 cells treated with E- and N-plasmid loaded CoMiP formulations compared to controls utilizing the traditional lipid transfection reagent, Lipofectamine$_{3000}$ (LF$_{3000}$). CoMiP and LF$_{3000}$ transfection efficiencies were similar when delivering S-encoding plasmids, while CoMiP-mediated delivery was slightly less effective for the M plasmid. It should be noted that transfection efficiencies in our experiments were generally low for both CoMiP carriers and LF$_{3000}$ (<10% of the cell population) as we utilized a small concentration of delivered plasmid (~5 ng/mL). This was done to conserve the material during these initial screening studies, particularly for difficult-to-express constructs (e.g., M- and N-plasmids). Later experiments using the prioritized S-plasmid DNA confirm that significantly higher transfection efficiencies can be obtained at elevated plasmid concentrations. Nevertheless, in many cases, superior transgene production was observed for CoMiP-treated cells compared to LF$_{3000}$ treated analogues. For example, RAW264.7 cells incubated with S- and E-plasmid-loaded CoMiP formulations (CoMiP$_S$ and CoMiP$_E$) showed a 33- and 43-fold increase in antigen production relative to LF$_{3000}$-transfected controls, respectively (Figure 4E,F, black bars).

Parallel assays tested the potential for local, non-professional human lung epithelial cells (NL20) to express CoMiP delivered antigens. Similar to RAW264.7 macrophages, treated NL20 cells showed a significantly higher expression of S- and E-encoded antigens following transfection with plasmids delivered via CoMiP carriers over LF$_{3000}$ (Figure 4E,F, gray bars). During these experiments, we noted a marked decrease in cell density and change in cellular morphology for LF$_{3000}$-treated samples (Supporting Information Figure S3), which was not observed for cells transfected with CoMiP. This Lipofectamine-mediated cell stress also led to a reduction in the autofluorescence of RAW264.7 and NL20 cells transfected with LF$_{3000}$ delivered S-plasmids (see LF$_S$ in Figure 4E). Our observations add to a growing body of evidence indicating that cationic lipid transfection reagents, such as LF$_{3000}$, negatively impact growth, stress, and apoptotic signaling pathways in treated cells.[37−39] This has renewed interest in developing more innocuous transfection reagents, such as CoMiP carriers, that decrease off-target effects and minimize the impact of transfection-mediated toxicity.

3.4. Dose Optimization and In Vivo Vaccination. Before vaccinating mice, we first optimized the formulation of S-plasmid loaded CoMiP through several in vitro assays. A dose ceiling was selected from tolerance studies performed in CoMiP-treated endothelial (HUVEC) and macrophage (THP-1) cell lines. The results in Figure 5A show that >80% viability of both cell lines was maintained at particle concentrations ≤0.01 mg/mL, establishing this as the dose maximum for in vivo immunization. Next, we explored the maximum concentration of S-encoding plasmids that could be efficiently loaded into the particles. S-plasmids were prioritized for these studies as they were successfully expressed in vitro following CoMiP delivery (Figure 4), are the primary antigens for currently deployed vaccines,[40,41] and, at the time of these experiments, were the only SARS-CoV-2 proteins for which commercial ELISA detection reagents were readily available.
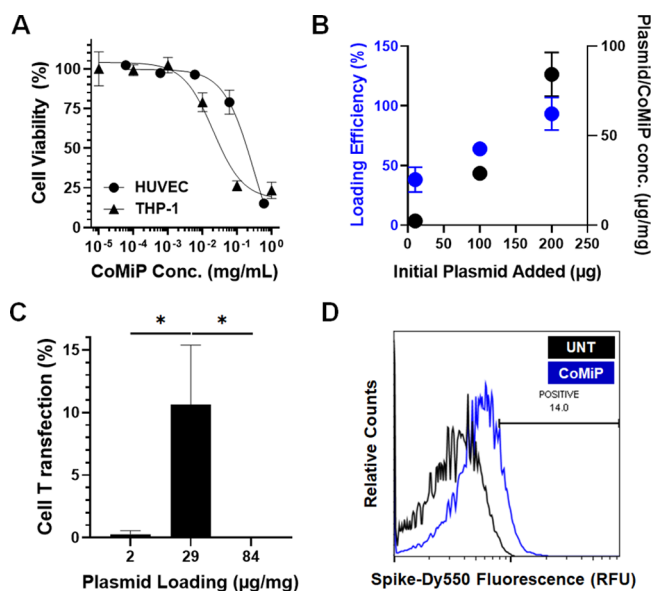
Figure 5. In vitro optimization of S-plasmid loaded CoMiP safety and efficacy. (A) Cytotoxicity of unloaded CoMiP toward HUVEC (●) and THP-1 (▲) cells following a 48 h incubation. (B) S-plasmid encapsulation as a function of total pDNA available in particle formulation. The results are shown as both pDNA loading efficiency (left, blue) and mass ratio of encapsulated plasmid to dry particle weight (right, black). (C) Relationship between $CoMiP_S$ plasmid loading and S-protein expression (transfection efficiency) in RAW264.7 murine macrophages. Statistical significance denoted by *$p \leq 0.05$. (D) Representative flow cytometry histograms of RAW264.7 macrophages before (untreated, black) and after a 72 h incubation with 29 μg/mg S-plasmid loaded $CoMiP_S$ (blue).

Interestingly, the CoMiP plasmid encapsulation efficiency increased linearly with vector concentration (Figure 5B). For example, the loading efficiency increased from 38% at 10 μg of total available plasmid, to 93% at 200 μg. The latter condition corresponds to 84 μg of plasmid encapsulated per mg of particle or ~8% of the total dry weight. One likely explanation is that increasing the concentration of plasmid available to complex with PLL decreases the probability of off-pathway interactions of free PLL with HA to form unloaded polyplexes. Our results also suggest that CoMiP can encapsulate large quantities of plasmids, the empirical maximum of which could not be attained in our studies due to constraints on plasmid production.

Interestingly, however, we observed that cell transfection efficiency did not increase monotonically with $CoMiP_S$ pDNA loading (Figure 5C,D). While increasing the plasmid load from 2 to 29 μg per mg of particles led to a 28-fold increase in transfection efficiency, a further increase to 84 μg/mg led to a complete loss of transgene production (Figure 5C, Supporting Information Figure S4). While the exact mechanism behind this counter-intuitive result is unknown, we can speculate two potential causes. First, increasing the amount of encapsulated plasmid leads to a concomitant increase of the plasmid/PLL ratio, the result of which is a greater propensity for the endosomolytic peptide to be sequestered within polyplexes. This would decrease the amount of free PLL available to permeate endosomes and enable cytoplasmic delivery of the plasmid cargo. Further support for this assertion comes from our prior studies monitoring the intracellular transport of HA-based nanoparticles.[19] During prior formulation of HA/PLL

ionic nanoparticles for protein delivery, we found that an N/P ratio of 10 (N = negative moieties of HA; P = positive moieties of PLL) led to efficient endosomal escape in A549 lung carcinoma cells. Calculating an analogous N/P ratio for $CoMiP_S$, where N now represents the number of negative charges from the plasmid, demonstrates that the 29 μg/mg particle formulation represents an N/P = 10. In addition to these material-specific factors, macrophages are uniquely adept at recognizing foreign nucleic acids and expressing intracellular DNAses in response.[42,43] High concentrations of plasmid delivered to the cytoplasm of macrophages could potently activate these mechanisms to, counter-productively, promote rapid clearance of the delivered pDNA. In sum, these studies identify 29 μg/mg plasmid loading as our lead formulation for follow-up in vivo immunization experiments.

To test the efficacy of our inhalable $CoMiP_S$ vaccines, C57BL/6 mice were immunized via intranasal installation of a 40 μL volume of 29 μg/mg $CoMiP_S$ in sterile saline. Control animals received a similar volume of the saline vehicle. Animals were given a boost dose at the same concentration 2 weeks later. Systemic immune responses were then evaluated via ELISA performed on serum samples collected from animals 14 and 28 days after vaccination and boost, respectively. Quantification of S-protein-specific serum immunoglobulin G (IgG) showed no statistically significant change in systemic antibody levels between $CoMiP_S$-treated animals and controls at both sampling time points (Figure 6A). To explore local mucosal immune responses, we also collected BALF from immunized mice 30 days after vaccination to assess differences in the total and S-protein specific lung mucosal IgA (Figure 6B). While there was a significant increase in the total IgA for mice vaccinated with $CoMiP_S$, no statistically significant difference in S-protein specific IgA was detected between the vaccinated and control animals. Finally, histology performed on lung tissues collected at the end of the vaccination period indicated no overt signs of pulmonary inflammation (Figure 6C), which would otherwise present as extensive cell infiltration, septal thickening, and collapsed airways. This is particularly important as the low-molecular-weight HA (100 kDa) used to construct the CoMiP carrier, although essential for CD44 receptor targeting on macrophages,[44] can stimulate leukocyte infiltration to cause airway inflammation, hyper-responsiveness, and tissue remodeling.[45] The marked lack of inflammation observed in the $CoMiP_S$-treated lung tissues may be due, in part, to encumbrance of anionic HA by the particle polyplex.

4. CONCLUSIONS

Macrophages are key mediators of both innate and adaptive immunity. Chief among their many roles is the capacity for antigen presentation to T helper cells, ultimately initiating a cascade of adaptive immune responses. The lung tissue contains two distinct macrophage populations, alveolar and interstitial macrophages.[46] Alveolar macrophages are in close contact with the alveolar epithelium and thus serve as the first line of defense against invading pathogens or noxious stimuli. These cells then react to these environmental signals to reversibly alter their polarization from the naïve state (Mø) to pro-inflammatory (M1) or anti-inflammatory (M2) pheno-types.[47,48] It is this remarkable inflammatory plasticity, which specializes alveolar macrophages to rapidly react with invading pathogens, that implies their potential as targets for vaccination. This was the rationale that initiated the develop-
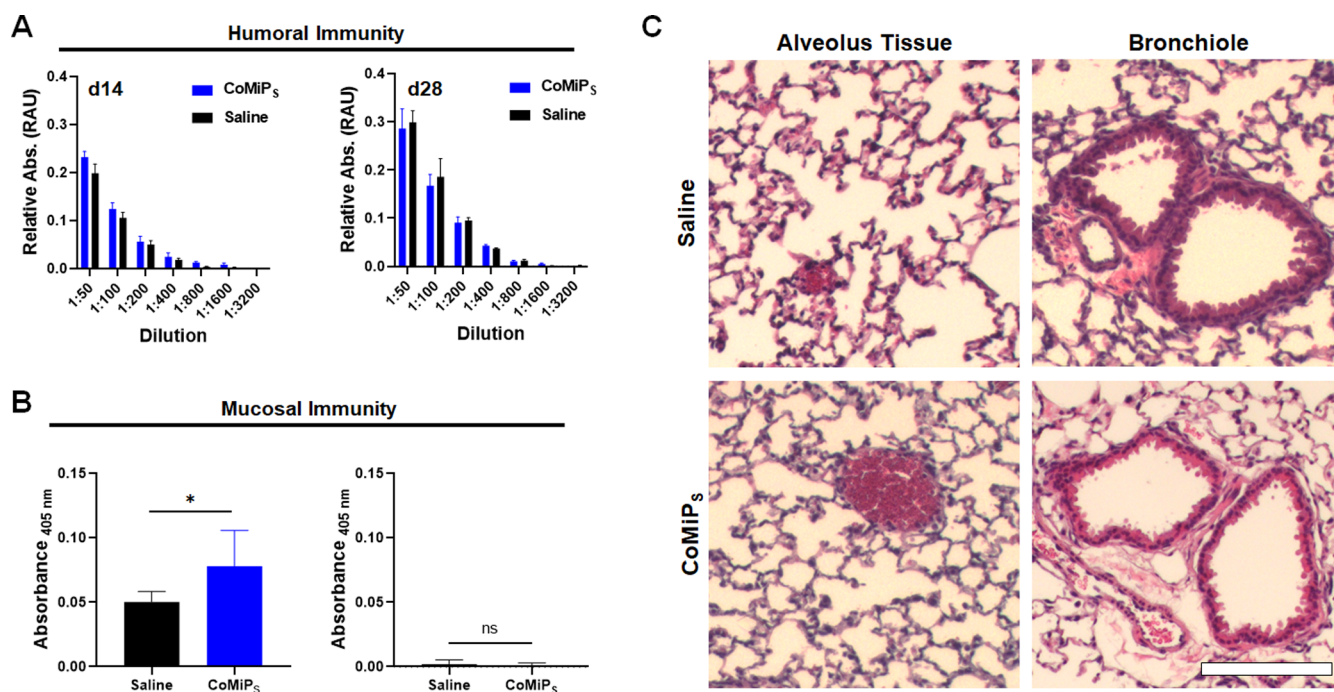
Figure 6. In vivo humoral and mucosal immune responses following vaccination with S-plasmid-loaded CoMiP (CoMiP$_S$) aerosols. Mice were primed on day 0 and boosted on day 14. (A) Quantification of systemic S-protein-specific IgG antibody titers in mouse serum 14 (left) and 28 days (right) after immunization with CoMiP$_S$ (blue) or blank saline (black) as a control. No statistical significance was observed between treatment groups. (B) Total (left) and S-specific (right) IgA antibody titers from BALF collected from mice immunized with CoMiP$_S$ (blue) or controls receiving saline (black). Statistical significance denoted by ns = not significant, $*p \leq 0.05$. (C) H&E-stained histologic lung tissue sections from mice immunized with CoMiP$_S$ or blank saline. Representative images for the alveolar tissue (left) and pulmonary bronchiole cross-sections (right) shown. Scale bar = 50 μm.

ment of our CoMiP inhalable vaccine platform against SARS-CoV-2. Yet, while S-protein encoded CoMiP$_S$ were able to effect robust and adaptable antigen production in vitro, they produced weak adaptive immune responses in vivo.

These contradictory results may be explained, in part, by recent work from the Tirelli group differentiating the cellular fate of HA particles in Mø, M1, and M2 macrophages.[49] First, they report that CD44 expression, the receptor responsible for binding HA, depends on macrophage polarization, with overall expression following the trend M1 > Mø ≥ M2. However, while CD44 expression positively correlated with HA particle binding, counter-intuitively, they showed that it negatively impacted cellular internalization. This intriguing result suggests that while a higher expression of CD44 (M1) allows more efficient capture of HA particles, a lower overall expression (M2) favors intracellular particle uptake. Thus, paradoxically, the cells most likely to bind HA-displaying CoMiP$_S$ may also be the most difficult to transfect with the nucleic acid payload due to their slower internalization of the carrier.

Additionally, the view that production of the antigenic protein at the site of infection should correlate to strong effector responses may be overly simplistic. It may be that trafficking of CoMiP$_S$ to the mucosa-associated lymphoid tissue, where the particles could then transfect specialized lymphoid cells, may produce stronger humoral and mucosal immune responses. Additionally, our formulations did not include an adjuvating molecule. Recent studies now indicate that presentation of the spike protein alone leads to poor immunogenic responses.[50] This suggests that inclusion of an adjuvant may strongly enhance the efficacy of the inhalable CoMiP platform.

Finally, evidence indicates that alveolar macrophages are not efficient in antigen presentation, particularly under resting conditions.[51] However, dendritic cells (DCs), another major player in adaptive immunity, are considered to be efficient antigen presenters[51] and participate in the early pathogenesis of SARS-CoV-2 infection.[52] Thus, redesigning CoMiP aerosols to additionally target surface receptors present on myeloid DCs represents a tractable complementary strategy. Further supporting this premise are studies indicating that aerosolized particles 200−300 nm in size, such as CoMiP, are optimal for uptake into DCs.[53] This would allow the carrier to exploit both macrophages and DCs for collaborative antigen cross-presentation to CD8$^+$ T lymphocytes and as a consequence more potent adaptive immune responses. Additional stimulation by pro-inflammatory macrophages leads to cross-priming of naive CD8$^+$ T lymphocytes to potentiate cytotoxic immunity. Moreover, evidence suggests that cross-priming may locally reactivate memory and effector T cells.[54] Therefore, co-stimulating macrophages and DCs to cross-present antigens delivered via CoMiP carriers may be a promising strategy for antiviral therapies as well. Similarly, co-delivery of antigen-encoding plasmids in combination with cytokines and co-stimulatory molecules is another fruitful avenue in the optimization of CoMiP aerosols. In sum, CoMiP carriers represent a versatile aerosolizable material that, with continued optimization and refinement, could lead to the development of safe and effective inhalable vaccines and therapies for SARS-CoV-2 and potentially other respiratory viruses.

■ ASSOCIATED CONTENT

ⓢ Supporting Information

The Supporting Information is available free of charge at https://pubs.acs.org/doi/10.1021/acs.biomac.1c01447.

Particle stability assays, CoMiP uptake into RAW264.7 macrophages, micrographs of transfected cells, and flow cytometry histogram of CoMiP$_S$-treated RAW 264.7 cells (PDF)

■ AUTHOR INFORMATION

Corresponding Author

Scott H. Medina − Department of Biomedical Engineering, Pennsylvania State University, University Park, Pennsylvania 16802-4400, United States; Huck Institutes of the Life Sciences, Penn State University, University Park, Pennsylvania 16802-4400, United States; Pennsylvania State University, University Park, Pennsylvania 16802-4400, United States; ⓞ orcid.org/0000-0001-5441-2164; Email: shm126@psu.edu

Authors

Atip Lawanprasert − Department of Biomedical Engineering, Pennsylvania State University, University Park, Pennsylvania 16802-4400, United States

Andrew W. Simonson − Department of Biomedical Engineering, Pennsylvania State University, University Park, Pennsylvania 16802-4400, United States

Sarah E. Sumner − Department of Veterinary and Biomedical Sciences, Pennsylvania State University, University Park, Pennsylvania 16802-4400, United States

McKayla J. Nicol − Department of Veterinary and Biomedical Sciences, Pennsylvania State University, University Park, Pennsylvania 16802-4400, United States

Sopida Pimcharoen − Department of Biomedical Engineering, Pennsylvania State University, University Park, Pennsylvania 16802-4400, United States

Girish S. Kirimanjeswara − Department of Veterinary and Biomedical Sciences, Center for Infectious Disease Dynamics, and Center for Molecular Immunology and Infectious Disease, Pennsylvania State University, University Park, Pennsylvania 16802-4400, United States

Complete contact information is available at:
https://pubs.acs.org/10.1021/acs.biomac.1c01447

Notes

The authors declare no competing financial interest.
The main data supporting the results in this study are available for research purposes from the corresponding authors on reasonable request.

■ ACKNOWLEDGMENTS

■ REFERENCES

(1) Wiersinga, W. J.; Rhodes, A.; Cheng, A. C.; Peacock, S. J.; Prescott, H. C. Pathophysiology, Transmission, Diagnosis, and Treatment of Coronavirus Disease 2019 (COVID-19): A Review. J. Am. Med. Assoc. 2020, 324, 782−793.

(2) Yuki, K.; Fujiogi, M.; Koutsogiannaki, S. COVID-19 pathophysiology: A review. Clin. Immunol. 2020, 215, 108427.

(3) Park, M. D. Macrophages: a Trojan horse in COVID-19? Nat. Rev. Immunol. 2020, 20, 351.

(4) Gómez-Rial, J.; Rivero-Calle, I.; Salas, A.; Martinón-Torres, F. Role of Monocytes/Macrophages in Covid-19 Pathogenesis: Implications for Therapy. Infect. Drug Resist. 2020, 13, 2485−2493.

(5) Meidaninikjeh, S.; Sabouni, N.; Marzouni, H. Z.; Bengar, S.; Khalili, A.; Jafari, R. Monocytes and macrophages in COVID-19: Friends and foes. Life Sci. 2021, 269, 119010.

(6) Hoffmann, M.; Kleine-Weber, H.; Schroeder, S.; Krüger, N.; Herrler, T.; Erichsen, S.; Schiergens, T. S.; Herrler, G.; Wu, N.-H.; Nitsche, A.; Müller, M. A.; Drosten, C.; Pöhlmann, S. SARS-CoV-2 Cell Entry Depends on ACE2 and TMPRSS2 and Is Blocked by a Clinically Proven Protease Inhibitor. Cell 2020, 181, 271−280.

(7) Liu, Z.; Xiao, X.; Wei, X.; Li, J.; Yang, J.; Tan, H.; Zhu, J.; Zhang, Q.; Wu, J.; Liu, L. Composition and divergence of coronavirus spike proteins and host ACE2 receptors predict potential intermediate hosts of SARS-CoV-2. J. Med. Virol. 2020, 92, 595−601.

(8) Song, X.; Hu, W.; Yu, H.; Zhao, L.; Zhao, Y.; Zhao, X.; Xue, H.-H.; Zhao, Y. Little to no expression of angiotensin-converting enzyme-2 on most human peripheral blood immune cells but highly expressed on tissue macrophages. Cytometry, Part A 2020. DOI: 10.1002/cyto.a.24285

(9) Feng, Z.; Diao, B.; Wang, R.; Wang, G.; Wang, C.; Tan, Y.; Liu, L.; Wang, C.; Liu, Y.; Liu, Y.; Yuan, Z.; Ren, L.; Wu, Y.; Chen, Y. The Novel Severe Acute Respiratory Syndrome Coronavirus 2 (SARS-CoV-2) Directly Decimates Human Spleens and Lymph Nodes, medRxiv 2020.03.27.20045427. Submitted 2020-03-31. medRxiv (COVID-19 SARS-CoV-2). 20045427. (accessed 2021-10-20).

(10) Gracia-Hernandez, M.; Sotomayor, E. M.; Villagra, A. Targeting macrophages as a therapeutic option in COVID-19. Front. Pharmacol. 2020, 11, 1659.

(11) Liao, M.; Liu, Y.; Yuan, J.; Wen, Y.; Xu, G.; Zhao, J.; Cheng, L.; Li, J.; Wang, X.; Wang, F.; Liu, L.; Amit, I.; Zhang, S.; Zhang, Z. Single-cell landscape of bronchoalveolar immune cells in patients with COVID-19. Nat. Med. 2020, 26, 842−844.

(12) Grant, R. A.; Morales-Nebreda, L.; Morales-Nebreda, L.; Markov, N. S.; Swaminathan, S.; Querrey, M.; Guzman, E. R.; Abbott, D. A.; Donnelly, H. K.; Donayre, A.; Goldberg, I. A.; Klug, Z. M.; Borkowski, N.; Lu, Z.; Kihshen, H.; Politanska, Y.; Sichizya, L.; Kang, M.; Shilatifard, A.; Qi, C.; Lomasney, J. W.; Argento, A. C.; Kruser, J. M.; Malsin, E. S.; Pickens, C. O.; Smith, S. B.; Walter, J. M.; Pawlowski, A. E.; Schneider, D.; Nannapaneni, P.; Abdala-Valencia, H.; Bharat, A.; Gottardi, C. J.; Budinger, G. R. S.; Misharin, A. V.; Singer, B. D.; Wunderink, R. G.; Morales-Nebreda, L.; Markov, N. S.; Swaminathan, S.; Querrey, M.; Guzman, E. R.; Abbott, D. A.; Donnelly, H. K.; Donayre, A.; Goldberg, I. A.; Klug, Z. M.; Borkowski, N.; Lu, Z.; Kihshen, H.; Politanska, Y.; Sichizya, L.; Kang, M.; Shilatifard, A.; Qi, C.; Lomasney, J. W.; Argento, A. C.; Kruser, J. M.; Malsin, E. S.; Pickens, C. O.; Smith, S. B.; Walter, J. M.; Pawlowski, A. E.; Schneider, D.; Nannapaneni, P.; Abdala-Valencia, H.; Bharat, A.; Gottardi, C. J.; Budinger, G. R. S.; Misharin, A. V.; Singer, B. D.; Wunderink, R. G.; Wagh, A. A.; Hauser, A. R.; Wolfe, A. R.; Thakrar, A.; Yeldandi, A. V.; Wang, A. A.; Levenson, A. R.; Joudi, A. M.; Tran, B.; Gao, C. A.; Kurihara, C.; Schroedl, C. J.; Horvath, C. M.; Meza, D.; Odell, D. D.; Kamp, D. W.; Winter, D. R.; Ozer, E. A.; Shanes, E. D.; Bartom, E. T.; Rendleman, E. J.; Leibenguth, E. M.; Wehbe, F.; Liu, G. Y.; Gadhvi, G. T.; Navarro, H. T.; Sznajder, J. I.; Dematte, J. E.; Le, J.; Arnold, J. M.; Du, J. C.; Coleman, J.; Bailey, J. I.; Deters, J. S.; Fiala, J. A.; Starren, J.; Ridge, K. M.; Secunda, K.; Aren, K.; Gates, K. L.; Todd, K.; Gradone, L. D.; Textor, L. N.; Wolfe, L. F.; Pesce, L. L.; Nunes Amaral, L. A.; Rosenbaum, M. L.; Kandpal, M.; Jain, M.; Sala, M. A.; Saine, M.; Carns, M.; Alexander, M. J.; Cuttica, M. J.;

Prickett, M. H.; Khan, N. H.; Chandel, N. S.; Soulakis, N. D.; Rivas, O. R.; Seed, P. C.; Reyfman, P. A.; Go, P. D.; Sporn, P. H. S.; Cooper, P. R.; Tomic, R.; Patel, R.; Garza-Castillon, R.; Kalhan, R.; Morimoto, R. I.; Mylvaganam, R. J.; Kim, S. S.; Gatesy, S. W. M.; Thakkar, S.; Ben Maamar, S.; Han, S.; Rosenberg, S. R.; Nozick, S.; Green, S. J.; Russell, S. R.; Poor, T. A.; Zak, T. J.; Lombardo, T. A.; Stoeger, T.; Shamaly, T.; Ren, Z. Circuits between infected macrophages and T cells in SARS-CoV-2 pneumonia. *Nature* **2021**, *590*, 635−641.

(13) Price, J. V.; Vance, R. E. The macrophage paradox. *Immunity* **2014**, *41*, 685−693.

(14) Kammona, O.; Bourganis, V.; Karamanidou, T.; Kiparissides, C. Recent developments in nanocarrier-aided mucosal vaccination. *Nanomedicine* **2017**, *12*, 1057−1074.

(15) Hellfritzsch, M.; Scherließ, R. Mucosal vaccination via the respiratory tract. *Pharmaceutics* **2019**, *11*, 375.

(16) Zheng, B.; Peng, W.; Guo, M.; Huang, M.; Gu, Y.; Wang, T.; Ni, G.; Ming, D. Inhalable nanovaccine with biomimetic coronavirus structure to trigger mucosal immunity of respiratory tract against COVID-19. *Chem. Eng. J.* **2021**, *418*, 129392.

(17) Lu, B.; Huang, Y.; Huang, L.; Li, B.; Zheng, Z.; Chen, Z.; Chen, J.; Hu, Q.; Wang, H. Effect of mucosal and systemic immunization with virus-like particles of severe acute respiratory syndrome coronavirus in mice. *Immunology* **2010**, *130*, 254−261.

(18) Rajapaksa, A. E.; Ho, J. J.; Qi, A.; Bischof, R.; Nguyen, T.-H.; Tate, M.; Piedrafita, D.; McIntosh, M. P.; Yeo, L. Y.; Meeusen, E.; Coppel, R. L.; Friend, J. R. Effective pulmonary delivery of an aerosolized plasmid DNA vaccine via surface acoustic wave nebulization. *Respir. Res.* **2014**, *15*, 60.

(19) Simonson, A. W.; Lawanprasert, A.; Goralski, T. D. P.; Keiler, K. C.; Medina, S. H. Bioresponsive peptide-polysaccharide nanogels — A versatile delivery system to augment the utility of bioactive cargo. *Nanomedicine* **2019**, *17*, 391−400.

(20) Van Hoecke, L.; Job, E. R.; Saelens, X.; Roose, K. Bronchoalveolar Lavage of Murine Lungs to Analyze Inflammatory Cell Infiltration. *J. Visualized Exp.* **2017**, *123*, 55398.

(21) Kiss, B.; Kis, Z.; Pályi, B.; Kellermayer, M. S. Z. Topography, Spike Dynamics, and Nanomechanics of Individual Native SARS-CoV-2 Virions. *Nano Lett.* **2021**, *21*, 2675−2680.

(22) Caldas, L. A.; Carneiro, F. A.; Higa, L. M.; Monteiro, F. L.; da Silva, G. P.; da Costa, L. J.; Durigon, E. L.; Tanuri, A.; de Souza, W. Ultrastructural analysis of SARS-CoV-2 interactions with the host cell via high resolution scanning electron microscopy. *Sci. Rep.* **2020**, *10*, 16099.

(23) Lin, S.; Lee, C.-K.; Lee, S.-Y.; Kao, C.-L.; Lin, C.-W.; Wang, A.-B.; Hsu, S.-M.; Huang, L.-S. Surface ultrastructure of SARS coronavirus revealed by atomic force microscopy. *Cell. Microbiol.* **2005**, *7*, 1763−1770.

(24) Rios de la Rosa, J. M.; Pingrajai, P.; Pelliccia, M.; Spadea, A.; Lallana, E.; Gennari, A.; Stratford, I. J.; Rocchia, W.; Tirella, A.; Tirelli, N. Binding and Internalization in Receptor-Targeted Carriers: The Complex Role of CD44 in the Uptake of Hyaluronic Acid-Based Nanoparticles (siRNA Delivery). *Adv. Healthcare Mater.* **2019**, *8*, 1901182.

(25) Simonson, A. W.; Umstead, T. M.; Lawanprasert, A.; Klein, B.; Almarzooqi, S.; Halstead, E. S.; Medina, S. H. Extracellular matrix-inspired inhalable aerogels for rapid clearance of pulmonary tuberculosis. *Biomaterials* **2021**, *273*, 120848.

(26) Bus, T.; Traeger, A.; Schubert, U. S. The great escape: how cationic polyplexes overcome the endosomal barrier. *J. Mater. Chem. B* **2018**, *6*, 6904−6918.

(27) Heider, H.; Verca, S. B.; Rusconi, S.; Asmis, R. Comparison of Lipid-Mediated and Adenoviral Gene Transfer in Human Monocyte-Derived Macrophages and COS-7 Cells. *BioTechniques* **2000**, *28*, 260−270.

(28) Tang, X.; Aljahdali, B.; Alasiri, M.; Bamashmous, A.; Cao, F.; Dibart, S.; Salih, E. A method for high transfection efficiency in THP-1 suspension cells without PMA treatment. *Anal. Biochem.* **2018**, *544*, 93−97.

(29) *ATCC Transfection Protocol for THP-1 Cells*, 2011. 08-05-11.

(30) Schnoor, M.; Buers, I.; Sietmann, A.; Brodde, M. F.; Hofnagel, O.; Robenek, H.; Lorkowski, S. Efficient non-viral transfection of THP-1 cells. *J. Immunol. Methods* **2009**, *344*, 109−115.

(31) Kusumawati, A.; Commes, T.; Liautard, J. P.; Widada, J. S. Transfection of myelomonocytic cell lines: cellular response to a lipid-based reagent and electroporation. *Anal. Biochem.* **1999**, *269*, 219−221.

(32) Wu, K.; Zhao, X.-j.; Wong, K.-w.; Fan, X.-y. Comparison of plasmid DNA versus PCR amplified gene of insert DNA for nucleofection in Kasumi-1 cells. *Cytotechnology* **2015**, *67*, 275−283.

(33) Satarker, S.; Nampoothiri, M. Structural proteins in severe acute respiratory syndrome coronavirus-2. *Arch. Med. Res.* **2020**, *51*, 482−491.

(34) Gordon, D. E.; Jang, G. M.; Bouhaddou, M.; Xu, J.; Obernier, K.; White, K. M.; O'Meara, M. J.; Rezelj, V. V.; Guo, J. Z.; Swaney, D. L.; Tummino, T. A.; Hüttenhain, R.; Kaake, R. M.; Richards, A. L.; Tutuncuoglu, B.; Foussard, H.; Batra, J.; Haas, K.; Modak, M.; Kim, M.; Haas, P.; Polacco, B. J.; Braberg, H.; Fabius, J. M.; Eckhardt, M.; Soucheray, M.; Bennett, M. J.; Cakir, M.; McGregor, M. J.; Li, Q.; Meyer, B.; Roesch, F.; Vallet, T.; Mac Kain, A.; Miorin, L.; Moreno, E.; Naing, Z. Z. C.; Zhou, Y.; Peng, S.; Shi, Y.; Zhang, Z.; Shen, W.; Kirby, I. T.; Melnyk, J. E.; Chorba, J. S.; Lou, K.; Dai, S. A.; Barrio-Hernandez, I.; Memon, D.; Hernandez-Armenta, C.; Lyu, J.; Mathy, C. J. P.; Perica, T.; Pilla, K. B.; Ganesan, S. J.; Saltzberg, D. J.; Rakesh, R.; Liu, X.; Rosenthal, S. B.; Calviello, L.; Venkataramanan, S.; Liboy-Lugo, J.; Lin, Y.; Huang, X.-P.; Liu, Y.; Wankowicz, S. A.; Bohn, M.; Safari, M.; Ugur, F. S.; Koh, C.; Savar, N. S.; Tran, Q. D.; Shengjuler, D.; Fletcher, S. J.; O'Neal, M. C.; Cai, Y.; Chang, J. C. J.; Broadhurst, D. J.; Klippsten, S.; Sharp, P. P.; Wenzell, N. A.; Kuzuoglu-Ozturk, D.; Wang, H.-Y.; Trenker, R.; Young, J. M.; Cavero, D. A.; Hiatt, J.; Roth, T. L.; Rathore, U.; Subramanian, A.; Noack, J.; Hubert, M.; Stroud, R. M.; Frankel, A. D.; Rosenberg, O. S.; Verba, K. A.; Agard, D. A.; Ott, M.; Emerman, M.; Jura, N.; von Zastrow, M.; Verdin, E.; Ashworth, A.; Schwartz, O.; d'Enfert, C.; Mukherjee, S.; Jacobson, M.; Malik, H. S.; Fujimori, D. G.; Ideker, T.; Craik, C. S.; Floor, S. N.; Fraser, J. S.; Gross, J. D.; Sali, A.; Roth, B. L.; Ruggero, D.; Taunton, J.; Kortemme, T.; Beltrao, P.; Vignuzzi, M.; García-Sastre, A.; Shokat, K. M.; Shoichet, B. K.; Krogan, N. J. A SARS-CoV-2 protein interaction map reveals targets for drug repurposing. *Nature* **2020**, *583*, 459−468.

(35) Ou, X.; Liu, Y.; Lei, X.; Li, P.; Mi, D.; Ren, L.; Guo, L.; Guo, R.; Chen, T.; Hu, J.; Xiang, Z.; Mu, Z.; Chen, X.; Chen, J.; Hu, K.; Jin, Q.; Wang, J.; Qian, Z. Characterization of spike glycoprotein of SARS-CoV-2 on virus entry and its immune cross-reactivity with SARS-CoV. *Nat. Commun.* **2020**, *11*, 1620.

(36) Chan, K. K.; Dorosky, D.; Sharma, P.; Abbasi, S. A.; Dye, J. M.; Kranz, D. M.; Herbert, A. S.; Procko, E. Engineering human ACE2 to optimize binding to the spike protein of SARS coronavirus 2. *Science* **2020**, *369*, 1261−1265.

(37) Yu, X.; Liang, X.; Xie, H.; Kumar, S.; Ravinder, N.; Potter, J.; de Mollerat du Jeu, X.; Chesnut, J. D. Improved delivery of Cas9 protein/gRNA complexes using lipofectamine CRISPRMAX. *Biotechnol. Lett.* **2016**, *38*, 919−929.

(38) Fiszer-Kierzkowska, A.; Vydra, N.; Wysocka-Wycisk, A.; Kronekova, Z.; Jarząb, M.; Lisowska, K. M.; Krawczyk, Z. Liposome-based DNA carriers may induce cellular stress response and change gene expression pattern in transfected cells. *BMC Mol. Biol.* **2011**, *12*, 27.

(39) Li, Z.; Zhang, C.; Wang, Z.; Shen, J.; Xiang, P.; Chen, X.; Nan, J.; Lin, Y. Lipofectamine 2000/siRNA complexes cause endoplasmic reticulum unfolded protein response in human endothelial cells. *J. Cell. Physiol.* **2019**, *234*, 21166−21181.

(40) Creech, C. B.; Walker, S. C.; Samuels, R. J. SARS-CoV-2 Vaccines. *J. Am. Med. Assoc.* **2021**, *325*, 1318−1320.

(41) Kyriakidis, N. C.; López-Cortés, A.; González, E. V.; Grimaldos, A. B.; Prado, E. O. SARS-CoV-2 vaccines strategies: a comprehensive review of phase 3 candidates. *npj Vaccines* **2021**, *6*, 28.

(42) Hirayama, D.; Iida, T.; Nakase, H. The Phagocytic Function of Macrophage-Enforcing Innate Immunity and Tissue Homeostasis. *Int. J. Mol. Sci.* **2017**, *19*, 92.

(43) Stacey, K. J.; Sester, D. P.; Sweet, M. J.; Hume, D. A. Macrophage activation by immunostimulatory DNA. *Curr. Top. Microbiol. Immunol.* **2000**, *247*, 41−58.

(44) Cyphert, J. M.; Trempus, C. S.; Garantziotis, S. Size Matters: Molecular Weight Specificity of Hyaluronan Effects in Cell Biology. *Int. J. Cell Biol.* **2015**, *2015*, 563818.

(45) Garantziotis, S.; Brezina, M.; Castelnuovo, P.; Drago, L. The role of hyaluronan in the pathobiology and treatment of respiratory disease. *Am. J. Physiol.* **2016**, *310*, L785−L795.

(46) Hu, G.; Christman, J. W. Editorial: Alveolar Macrophages in Lung Inflammation and Resolution. *Front. Immunol.* **2019**, *10*, 2275.

(47) Ariel, A.; Maridonneau-Parini, I.; Rovere-Querini, P.; Levine, J. S.; Mühl, H. Macrophages in inflammation and its resolution. *Front. Immunol.* **2012**, *3*, 324.

(48) Herold, S.; Mayer, K.; Lohmeyer, J. Acute Lung Injury: How Macrophages Orchestrate Resolution of Inflammation and Tissue Repair. *Front. Immunol.* **2011**, *2*, 65.

(49) Rios de la Rosa, J. M.; Tirella, A.; Gennari, A.; Stratford, I. J.; Tirelli, N. The CD44-Mediated Uptake of Hyaluronic Acid-Based Carriers in Macrophages. *Adv. Healthcare Mater.* **2017**, *6*, 1601012.

(50) Wørzner, K.; Sheward, D. J.; Schmidt, S. T.; Hanke, L.; Zimmermann, J.; McInerney, G.; Hedestam, G. B. K.; Murrell, B.; Christensen, D.; Pedersen, G. K. Adjuvanted SARS-CoV-2 spike protein elicits neutralizing antibodies and CD4 T cell responses after a single immunization in mice. *EBioMedicine* **2021**, *63*, 103197.

(51) Nicod, L. P.; Cochand, L.; Dreher, D. Antigen presentation in the lung: dendritic cells and macrophages. *Sarcoidosis Vasc. Diffuse Lung Dis.* **2000**, *17*, 246−255.

(52) Campana, P.; Parisi, V.; Leosco, D.; Bencivenga, D.; Della Ragione, F.; Borriello, A. Dendritic cells and SARS-CoV-2 infection: still an unclarified connection. *Cells* **2020**, *9*, 2046.

(53) Rietscher, R.; Schröder, M.; Janke, J.; Czaplewska, J.; Gottschaldt, M.; Scherließ, R.; Hanefeld, A.; Schubert, U. S.; Schneider, M.; Knolle, P. A. Antigen delivery via hydrophilic PEG-b-PAGE-b-PLGA nanoparticles boosts vaccination induced T cell immunity. *Eur. J. Pharm. Biopharm.* **2016**, *102*, 20−31.

(54) Muntjewerff, E. M.; Meesters, L. D.; Van Den Bogaart, G. Antigen cross-presentation by macrophages. *Front. Immunol.* **2020**, *11*, 1276.